# First-principles study of commensurate twisted MoS2/MoSe2 heterobilayers: Structural, electronic, and elastic properties

Yiming Ren(任一鸣), Xiaoyang Wu(吴晓阳), Junrong He(何俊荣), Zhenglong Hu(胡正龙), Chunbo Hua(花春波), Li Xue(薛丽)

**Citation:**Chin. Phys. B. 35, 107101 (2026). DOI: 10.1088/1674-1056/ae27b3 | CSTR: 32038.14.CPB.ae27b3
http://cpb.iphy.ac.cn; http://iopscience.iop.org/cpb

**What follows is a list of articles you may be interested in**

---

## Potential effect of the deformation of strong-coupling polaron in perovskite materials

Jing Bai(白静), Ran An(安然), Xin-Xue Zhang(张新雪), Hui-Yi Cai(蔡蕙翼), Xin-Xin Duan(段欣欣), Xin Zhang(张鑫), Xin-Jun Ma(马新军), Yong Sun(孙勇)
Chin. Phys. B. 35, 097101 (2026). DOI: 10.1088/1674-1056/ae1c20 | CSTR: 32038.14.CPB.ae1c20

## Förster energy transfer boosts indirect anisotropic interlayer excitons in 2L-$MoSe_2$/perovskite heterostructures

Yingying Chen(陈瑛瑛), Zihao Jiao(焦子豪), Haizhen Wang(王海珍), Dehui Li(李德慧)
Chin. Phys. B. 35, 057112 (2026). DOI: 10.1088/1674-1056/ae5782 | CSTR: 32038.14.CPB.ae5782

## Bilayer twisting as a mean to isolate connected flat bands in a kagome lattice through Wigner crystallization

Jing Wu(吴静), Yue-E Xie(谢月娥), Ming-Xing Chen(陈明星), Jia-Ren Yuan(袁加仁), Xiao-Hong Yan(颜晓红), Sheng-Bai Zhang(张绳百), Yuan-Ping Chen(陈元平)
Chin. Phys. B. 30, 077104 (2021). DOI: 10.1088/1674-1056/abd7d6

## Tunable bandgaps and flat bands in twisted bilayer biphenylene carbon

Ya-Bin Ma(马亚斌), Tao Ouyang(欧阳滔), Yuan-Ping Chen(陈元平), Yue-E Xie(谢月娥)
Chin. Phys. B. 30, 077103 (2021). DOI: 10.1088/1674-1056/ac009e

## Density wave and topological superconductivity in the magic-angle-twisted bilayer-graphene

Ming Zhang(张铭), Yu Zhang(张渝), Chen Lu(卢晨), Wei-Qiang Chen(陈伟强), Fan Yang(杨帆)
Chin. Phys. B. 29, 127102 (2020). DOI: 10.1088/1674-1056/abc7b5

---

# First-principles study of commensurate twisted $MoS_2/MoSe_2$ heterobilayers: Structural, electronic, and elastic properties

Yiming Ren(任一鸣)[1], Xiaoyang Wu(吴晓阳)[1], Junrong He(何俊荣)[1,2], Zhenglong Hu(胡正龙)[1,2], Chunbo Hua(花春波)[1,2], and Li Xue(薛丽)[1,2,†]

[1] *School of Electronic and Information Engineering, Hubei University of Science and Technology, Xianning* 437100, *China*
[2] *Key Laboratory of Photoelectronic Sensing and Intelligent Control, Hubei University of Science and Technology, Xianning* 437100, *China*

(Received 24 September 2025; revised manuscript received 2 December 2025; accepted manuscript online 4 December 2025)

This study investigates the structural, electronic and elastic properties of commensurate twisted $MoS_2/MoSe_2$ heterobilayers across five specific twist angles through first-principles calculations. We identify a critical angle (30°) that yields an exceptionally flat interface, characterized by a minimal interlayer spacing variation of only 0.017 Å. This distinctive planar morphology originates from a high-symmetry moiré superlattice with spatially uniform stacking configurations. Furthermore, we reveal that the variation in interlayer binding energy is governed by the lattice corrugation, reflected by a larger difference between maximum and minimum bilayer thicknesses. A more pronounced corrugation enables the system to maximize the fractional area of strongly coupled, low-energy stacking domains (e.g., AB-1) while minimizing that of weakly coupled, high-energy regions (e.g., AA). Electronically, the system exhibits a twist-angle-dependent transition between direct and indirect band gaps, while maintaining a robust type-II band alignment across all angles, with band edges localized in the $MoSe_2$ and $MoS_2$ layers, respectively. Elastic properties remain nearly unchanged at twist angles greater than 9°, but the Young's moduli of these heterobilayers surpass those of silicene and phosphorene. These findings highlight the potential of twisted $MoS_2/MoSe_2$ heterobilayers as a tunable platform for advanced optoelectronic devices.

**Keywords:** $MoS_2/MoSe_2$ heterobilayer, twist angle, electronic properties, elastic properties, first-principles

**PACS:** 71.15.Mb, 71.20.–b, 71.20.Nr

**DOI:** 10.1088/1674-1056/ae27b3 **CSTR:** 32038.14.CPB.ae27b3

## 1. Introduction

In recent years, moiré superlattices have attracted significant interest in condensed matter physics owing to the emergence of novel quantum phenomena induced by the moiré patterns formed through interlayer twisting. This research momentum has been driven largely by advances in van der Waals (vdW) materials,[1–3] which enable precise fabrication and atomic-scale characterization of such systems. Stacking two atomically thin two-dimensional (2D) crystals with a lattice mismatch or relative twist angle leads to the formation of long-range moiré superlattices, first experimentally visualized in graphene multilayers using scanning tunneling microscopy.[4] Such moiré periodicity induces atomic-scale interlayer coupling that profoundly modifies the electronic and optical properties of the system, giving rise to emergent behaviors that are absent in the constituent monolayers.[5–8]

Among various 2D systems, transition metal dichalcogenides (TMDs) have attracted widespread attention in the field of 2D materials research due to their unique layered structure and tunable chemical, physical, and mechanical properties.[9–12] Especially in twisted TMD systems, variations in the twist angle allow precise manipulation of interlayer coupling and stacking configuration, leading to the emergence of a wide array of correlated electronic behaviors, including Mott insulating states, superconductivity, and interlayer exciton physics.[13–15]

While moiré phenomena in twisted TMD bilayers have been studied for over a decade, the critical role of lattice relaxation was highlighted only recently. In 2021, Angeli and MacDonald[16] reported the emergence of a Dirac cone after structural relaxation, underscoring its importance. Subsequently, Vitale *et al.*[17] performed classical force-field relaxations of twisted TMD homo- and heterostructures and computed electronic structures using a tight-binding model parameterized with density functional theory (DFT). Their work revealed qualitatively different band structures when relaxations were neglected, attributing this to both in-plane rearrangement and out-of-plane corrugation. Similar reconstruction effects have been observed by simulations in systems including graphene[18], $MoS_2$[19] and $MoS_2/WSe_2$,[20] as well as through experimental evidence.[21]

A major challenge in simulating such systems arises from the incommensurability of heterobilayers under arbitrary twists, which complicates the application of periodic boundary conditions in conventional DFT or force-field methods.[22] To overcome this, the coincidence lattice method[23–25] has been developed to identify specific twist angles yielding commensurate moiré superlattices. This approach searches for perfect

[†]Corresponding author. E-mail: xueli0610@163.com

© 2026 Chinese Physical Society and IOP Publishing Ltd. All rights, including for text and data mining, AI training, and similar technologies, are reserved.

lattice coincidence between the top and bottom layers, sometimes assisted by minimal strain to achieve practical supercell sizes.[25] Although Naik *et al.*[23] introduced a generalized framework for constructing and relaxing commensurate superlattices across various 2D materials, a systematic investigation of the structural, electronic and elastic properties of commensurate superlattices remains lacking.

Inspired by these advances, we construct a series of commensurate $MoS_2$/$MoSe_2$ heterobilayers with five specific twist angles (9.18°, 16.1°, 30°, 43.9° and 50.82°) using the coincidence lattice method, followed by full structural relaxation. Using first-principles calculations, we comprehensively characterize their structural, electronic and elastic properties. Our results reveal the twist-angle dependence in interlayer spacing variation, binding energy, energy band structure and elastic moduli. These insights not only deepen our understanding of twisted TMD systems but also provide valuable guidance for the design of advanced optoelectronic devices.

## 2. Methods

### 2.1. The method of constructing twisted heterobilayers

The construction of commensurate twisted heterobilayers requires identifying a common superlattice period for both layers. We follow the coincidence site lattice theory, as formalized by Naik *et al.*,[23] to generate these structures. For a heterobilayer composed of two different hexagonal lattices, we define the primitive lattice vectors for the bottom layer as $\boldsymbol{a}_1 = a(\frac{\sqrt{3}}{2}\boldsymbol{i} - \frac{1}{2}\boldsymbol{j})$ and $\boldsymbol{a}_2 = a(\frac{\sqrt{3}}{2}\boldsymbol{i} + \frac{1}{2}\boldsymbol{j})$, and for the top layer as $\boldsymbol{b}_1 = b(\frac{\sqrt{3}}{2}\boldsymbol{i} - \frac{1}{2}\boldsymbol{j})$ and $\boldsymbol{b}_2 = b(\frac{\sqrt{3}}{2}\boldsymbol{i} + \frac{1}{2}\boldsymbol{j})$, where $a$ and $b$ are the respective lattice constants and $\boldsymbol{i}$ and $\boldsymbol{j}$ denote the unit vector along the $x$- and $y$-axes in a Cartesian coordinate system. In a twisted heterobilayer, the layers are rotated relative to each other. To ensure that the angles between the superlattice vectors of the bottom and top layers are 60°, the superlattice vectors $\boldsymbol{A}_1$, $\boldsymbol{A}_2$ for the bottom layer and $\boldsymbol{B}_1$, $\boldsymbol{B}_2$ for the top layer are related to their primitive vectors by

$$\begin{pmatrix} \boldsymbol{A}_1 \\ \boldsymbol{A}_2 \end{pmatrix} = \begin{pmatrix} n_1 & n_2 \\ -n_2 & n_1+n_2 \end{pmatrix} \begin{pmatrix} \boldsymbol{a}_1 \\ \boldsymbol{a}_2 \end{pmatrix}, \tag{1}$$

$$\begin{pmatrix} \boldsymbol{B}_1 \\ \boldsymbol{B}_2 \end{pmatrix} = \begin{pmatrix} m_1 & m_2 \\ -m_2 & m_1+m_2 \end{pmatrix} \begin{pmatrix} \boldsymbol{b}_1 \\ \boldsymbol{b}_2 \end{pmatrix}, \tag{2}$$

where $n_1$, $n_2$, $m_1$ and $m_2$ are integers. The corresponding twist angle $\theta$ can be solved by $\boldsymbol{A}_1 \cdot \boldsymbol{B}_1 = |\boldsymbol{A}_1||\boldsymbol{B}_1|\cos\theta$. The twist angle $\theta$ satisfies the equation

$$\cos\theta = \frac{3(n_1+n_2)(m_1+m_2)+(n_1-n_2)(m_1-m_2)}{4\sqrt{n_1^2+n_1n_2+n_2^2}\sqrt{m_1^2+m_1m_2+m_2^2}}. \tag{3}$$

The number of unit cells $N$ in the superlattice is characterized by the four integers, $n_1$, $n_2$, $m_1$ and $m_2$

$$N = n_{\text{atom}}(n_1^2+n_1n_2+n_2^2) + m_{\text{atom}}\left(m_1^2+m_1m_2+m_2^2\right), \tag{4}$$

where $n_{\text{atom}}$ and $m_{\text{atom}}$ represent the number of atoms in the primitive cells for the bottom and top layers, respectively.

For homolayers with identical lattice constants ($a = b$), the commensurability condition requires the equivalence of corresponding superlattice vectors between the bottom and top layers, i.e., $|\boldsymbol{A}_1| = |\boldsymbol{B}_1|$. We can obtain many sets of solutions, among which $m_1 = n_2$ and $m_2 = n_1$ are one. Substituting these constraints into Eq. (3), the twist angle expression simplifies to

$$\cos\theta = \frac{n_1^2+4n_1n_2+n_2^2}{2(n_1^2+n_1n_2+n_2^2)}. \tag{5}$$

Equation (5) is consistent with the general form of twist angle reported by Uchida *et al.*[24] The specific case where $n_2 - n_1 = 1$ corresponds to a superlattice containing only one moiré stripe. By setting $n_1 = i$ and $n_2 = i+1$, where $i$ is an integer, the twist angle expression further reduces to

$$\cos\theta = \frac{3i^2+3i+0.5}{3i^2+3i+1}, \tag{6}$$

which matches the expression given by Lopes dos Santos *et al.*[26] This agreement confirms the validity and reliability of our derivation for the twist angle.

For heterobilayer systems, to manage inherent lattice mismatch ($a \neq b$), we introduce a tolerance threshold $\Delta$ (Å) to quantify the maximum permissible deviation between superlattice vector magnitudes

$$||\boldsymbol{A}_1| - |\boldsymbol{B}_1|| \leq \Delta. \tag{7}$$

For perfectly commensurate structures, we apply a minimal biaxial strain $\beta$ to both layers to achieve exact lattice matching, following the condition[25]

$$(1+\beta)\,|\boldsymbol{A}_1| \approx (1-\beta)\,|\boldsymbol{B}_1|. \tag{8}$$

### 2.2. Test system and examples

To validate the procedure described in Subsection 2.1, we consider the construction of twisted bilayer $MoS_2$ and twisted $MoS_2$/$MoSe_2$ heterobilayers as representative examples. For consistent comparison, the lattice parameters of $MoS_2$ and $MoSe_2$ during the testing process are set equal to those reported in Naik *et al.*[23] The initial stacking configuration for twisted bilayers at $\theta = 0°$ is defined as AA stacking, where both metal and chalcogen atoms in the top layer are positioned directly above their respective counterparts in the bottom layer. The transformation matrices for bilayer $MoS_2$ with $\theta = 27.8°$ and $MoS_2$/$MoSe_2$ with $\theta = 16.1°$ agree with those published by Naik *et al.*,[23] and the atom numbers are consistent with data in Refs. [23,27–29], as summarized in Table 1. This consistency confirms the accuracy of our modeling method for generating twisted heterobilayers.

**Table 1.** The twisted angle $\theta$, the transition matrix of the first $MoS_2$ layer $\boldsymbol{P}_1$, the transition matrix of the second $MoS_2$ or $MoSe_2$ layer $\boldsymbol{P}_2$, the number of atoms in the primitive cells $N$ and biaxial strain $\beta$.

| Materials | $\theta$ (°) | $\boldsymbol{P}_1$ | $\boldsymbol{P}_2$ | $N$ | $\beta$ |
|---|---|---|---|---|---|
| Bilayer $MoS_2$ | 27.8 | $\begin{pmatrix} -4 & 3 \\ -3 & -1 \end{pmatrix}$ [23] | $\begin{pmatrix} 3 & -4 \\ 4 & -1 \end{pmatrix}$ | 78 [23] | 0 |
| Bilayer $MoS_2$ | 21.79 | $\begin{pmatrix} 1 & -3 \\ 3 & -2 \end{pmatrix}$ | $\begin{pmatrix} 2 & -3 \\ 3 & -1 \end{pmatrix}$ | 42 [27] | 0 |
| Bilayer $MoS_2$ | 13.17 | $\begin{pmatrix} 2 & -5 \\ 5 & -3 \end{pmatrix}$ | $\begin{pmatrix} 3 & -5 \\ 5 & -2 \end{pmatrix}$ | 114 [27,28] | 0 |
| $MoS_2$/$MoSe_2$ | 16.1 | $\begin{pmatrix} -1 & -3 \\ 3 & -4 \end{pmatrix}$ [23] | $\begin{pmatrix} -2 & -2 \\ 2 & -4 \end{pmatrix}$ | 75 [23,29] | 0.118% |
| $MoS_2$/$MoSe_2$ | 43.9 | $\begin{pmatrix} 1 & -4 \\ 4 & -3 \end{pmatrix}$ | $\begin{pmatrix} -2 & -2 \\ 2 & -4 \end{pmatrix}$ | 75 [29] | 0.118% |

### 2.3. Computational setup

Structural optimizations are performed to determine the equilibrium atomic structures of twisted $MoS_2$/$MoSe_2$ heterobilayers. These calculations employed the Broyden–Fletcher–Goldfarb–Shanno algorithm within a plane-wave pseudopotential framework based on DFT, using the CASTEP code.[30,31] The exchange–correlation energy is treated within the generalized gradient approximation as parameterized by Perdew, Burke and Ernzerhof.[32] Ion–electron interactions are described using Vanderbilt-type ultrasoft pseudopotentials.[33] To account for the vdW interactions between the two layers, the Grimme correction (DFT-D3) is employed.[34] A plane-wave energy cutoff of 500 eV is employed, and a $k$-point spacing of 0.04 Å$^{-1}$ is adopted for Brillouin zone sampling.[35] The convergence criteria are set as follows: energy tolerance of $1 \times 10^{-6}$ eV/atom, maximum force of 0.001 eV/Å, maximum stress of 0.002 GPa and maximum displacement of $5 \times 10^{-4}$ Å. To eliminate spurious interactions between periodic images, a vacuum layer of 15 Å is introduced along the [001] direction.

## 3. Results and discussion

### 3.1. Structural properties and binding energy

Both $MoS_2$ and $MoSe_2$ belong to the hexagonal crystal system. The optimized lattice parameters from our calculations are 3.186 Å for $MoS_2$ and 3.293 Å for $MoSe_2$, which are consistent with previously reported theoretical values.[23,29] We define six high-symmetry stacking configurations based on the vertical alignment of atomic species between the $MoS_2$ and $MoSe_2$ layers, as shown in Fig. 1. AA stacking refers to the configuration where Mo sits directly above Mo and S above Se. In contrast, $AA_1$ stacking features Mo above Se and S above Mo. The $A_1B$ registry is characterized by S above Se. In the $AB_1$ configuration, Mo is above Mo. Conversely, AB-1 stacking has S above Mo. Finally, the AB-2 configuration involves Mo above Se.

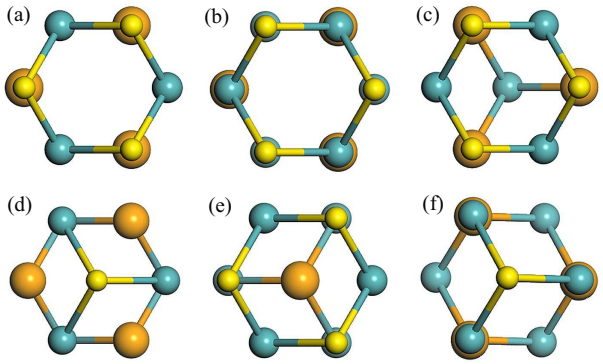


**Fig. 1.** Six high-symmetry stacking configurations between the $MoS_2$ and $MoSe_2$ layers: (a) AA, (b) AA1, (c) A1B, (d) AB1, (e) AB-1, (f) AB-2. Green, yellow and brown spheres represent Mo, S and Se atoms, respectively.

To maintain a balance between computational tractability and physical realism, we selected twist angles of 9.18°, 16.1°, 30°, 43.9° and 50.82° for $MoS_2$/$MoSe_2$ heterobilayers, ensuring that the resulting biaxial strain remained below 1%. As demonstrated by Arnold *et al.*[19] and Li *et al.*,[20] structural relaxation plays a critical role in determining both the in-plane and out-of-plane configurations. In accordance with these studies, we perform simultaneous optimization of the lattice parameters and atomic coordinates for twisted $MoS_2$/$MoSe_2$ heterobilayers. The optimized atomic structures corresponding to twist angles of 9.18°, 16.1° and 30° are illustrated in Fig. 2.

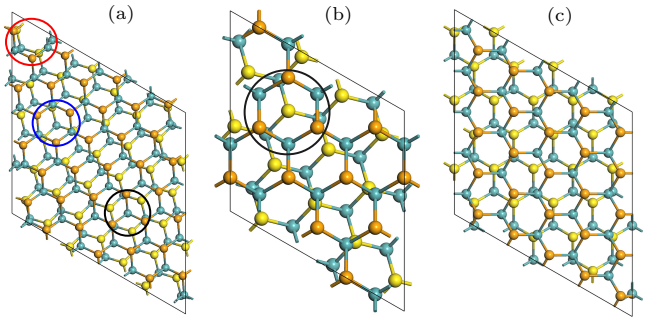


**Fig. 2.** Optimized atomic structures of $MoS_2$/$MoSe_2$ heterobilayers with twist angles of (a) 9.18°, (b) 16.1° and (c) 30°. AA, AB-1 and AB-2 are indicated by the red, green and black circles, respectively.

The maximum and minimum bilayer thicknesses, denoted as $d_{max}$ and $d_{min}$, and defined as the vertical separation between the Mo atoms in the two layers along the $z$-direction, are plotted as a function of twist angle $\theta$ in Fig. 3. Our results indicate that the variation in interlayer spacing ($\Delta d = d_{max} - d_{min}$) decreases from 0.255 Å at 9.18° to 0.017 Å at 30°. In contrast, as $\theta$ increases further from 30° to 50.82°, $\Delta d$ increases from 0.017 Å to 0.253 Å. The largest fluctuations in interlayer spacing occur at 9.18° and 50.82° ($\Delta d \approx 0.26$ Å) among the five twist angles in our study, reflecting significant atomic-level relaxations at the interface that lead to a corrugated morphology. Conversely, the heterobilayer at 30° exhibits remarkable interfacial flatness, with a minimal variation in interlayer

spacing ($\Delta d \approx 0.017$ Å), closely approximating an ideal planar interface. This contrast in flatness is directly attributable to the spatial distribution of local stacking configurations. At small twist angles such as 9.18°, the moiré superlattice exhibits large unit cells containing AA, AB-1 and AB-2 stacking, each favoring different equilibrium interlayer distances as displayed in Fig. 4. The competition among these regions induces out-of-plane distortions and leads to the observed corrugation. In contrast, at the 30° twist angle, the system forms a high-symmetry commensurate moiré superlattice characterized by a uniform atomic registry. This structural homogeneity means that each local region experiences similar local stacking environments and vdW adhesion energies. As a result, the system reaches a single global energy minimum, stabilizing a nearly planar geometry with a uniform interlayer separation. The pronounced dependence of $\Delta d$ on $\theta$ highlights the substantial out-of-plane deformation arising from atomic reconstruction during structural optimization,[19,20,27,36] proving the importance of incorporating out-of-plane relaxation in accurate structural models.

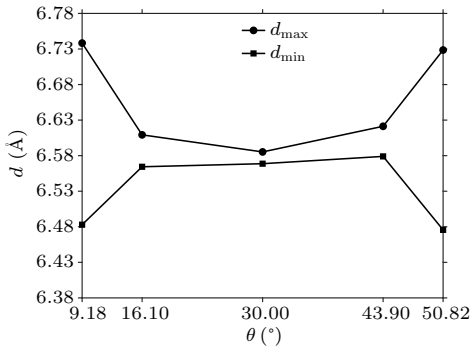


**Fig. 3.** Maximum ($d_{max}$) and minimum ($d_{min}$) bilayer thicknesses as a function of twist angle $\theta$.

To evaluate the stability of twisted $MoS_2/MoSe_2$ heterobilayers, the binding energy $E_b$ is calculated using the following formula:[37]

$$E_b = (E_{BL} - E_{ML,bottom} - E_{ML,top})/N, \quad (9)$$

where $N$ is the number of atoms in the moiré superlattice, $E_{BL}$ is the total energy of the heterobilayer and $E_{ML,i}$ is the total energy of each freestanding constituting monolayer. For comparison, we calculate the binding energies for non-relaxed structures across varying interlayer distances, as listed in Table 2. The binding energies for the non-relaxed structures show a minimum for each angle. The system with a twist angle of 30° exhibits the least negative binding energy across almost all interlayer distances in its non-relaxed state. After full relaxation, the binding energies of all twisted structures become significantly more negative. The highly corrugated systems (9.18° and 50.82°) optimize their energy by maximizing the area of low-energy stacking with a smaller interlayer distance. The large area of regions with small $d$ approximates the strong-coupling AB-1 and AB-2 stacking configurations (as shown in the binding energy in Fig. 4), which dominates and lowers the total energy. In contrast, the exceptionally flat 30° system has an extremely narrow range of interlayer distances ($d_{max} = 6.585$ Å, $d_{min} = 6.569$ Å). It cannot form large areas with small $d$ via lattice corrugation due to the symmetry constraint by formation of a much smaller commensurate moiré superlattice and thus cannot achieve binding as strong as the most stable AB-1 stacking. Instead, it minimizes its energy by forming a spatially uniform and moderately coupled stacking registry.

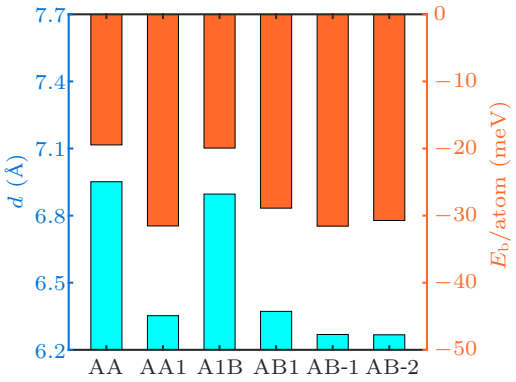


**Fig. 4.** The interlayer distance $d$ and the binding energy per atom $E_b$ (meV) of six high-symmetry stacking configurations of $MoS_2/MoSe_2$ heterobilayers.

**Table 2.** The binding energy per atom $E_b$ of non-relaxed structures across varying interlayer distances and the relaxed $MoS_2/MoSe_2$ heterobilayers with different twist angles.

| | $d$ (Å) | $\theta = 9.18°$ | $\theta = 16.1°$ | $\theta = 30°$ | $\theta = 43.9°$ | $\theta = 50.82°$ |
|---|---|---|---|---|---|---|
| Non-relaxed structures | 6.23 | –17.789 | –17.989 | –12.404 | –17.982 | –17.849 |
| | 6.48 | –23.823 | –23.843 | –16.377 | –23.744 | –23.752 |
| | 6.73 | –22.866 | –24.181 | –16.582 | –24.180 | –24.117 |
| | 6.98 | –22.121 | –21.943 | –15.035 | –21.943 | –21.897 |
| | 7.23 | –19.259 | –19.070 | –13.136 | –19.070 | –19.035 |
| Relaxed structures | | –25.417 | –24.820 | –24.744 | –24.781 | –25.419 |

Furthermore, both the interlayer distance and the binding energy exhibit an approximate symmetry with respect to $\theta = 30°$. The atomic configuration at a twist angle of 60°–$\theta$ can be obtained from that at $\theta$ by an in-plane translation of one layer following a mirror inversion of the entire structure. Since mirror symmetry preserves energy, the primary difference between configurations related by this operation reduces to a lateral shift. The resulting symmetry around $\theta = 30°$ in-

dicates that such translational differences have a negligible influence on the system's energetics and structural properties. This behavior is consistent with previous observations in other twisted bilayer systems such as graphene.[24]

### 3.2. Electronic properties

A systematic investigation of the energy band structures and density of states (DOS) is conducted to elucidate the electronic properties of twisted $MoS_2/MoSe_2$ heterobilayers. The calculated energy band structures for selected twist angles are shown in Figs. 5(a)–5(c), where the valence band maximum (VBM) is set to 0 eV. All heterobilayers exhibit semiconducting characteristics, with both direct and indirect band gaps being observed depending on the twist angle. Owing to the electronic similarity between structures with twist angles of 9.18° and 50.82°, and between 16.1° and 43.9°, only representative band structures for 9.18° and 16.1° are displayed in Fig. 5. The results indicate that heterobilayers with $\theta = 16.9°$ and 43.1° are indirect band gap semiconductors, with band gaps of 1.114 eV and 1.117 eV, respectively. As depicted in Fig. 5(b), the VBM is located at the $\Gamma$ point, while the conduction band minimum (CBM) lies at the $K$ point, consistent with previous reports.[29] In contrast, heterobilayers with $\theta =$ 9.18°, 30° and 50.82° exhibit direct band gap behavior, with band gaps of 1.030 eV, 1.103 eV and 1.023 eV, respectively. In these cases, both the VBM and CBM are situated at the $\Gamma$ point, as illustrated in Figs. 5(a) and 5(c). This behavior originates from the larger superlattice periods at these twist angles compared with that at 16.1°, which leads to a contraction of the Brillouin zone boundaries in reciprocal space. As a result, the energy bands of the primitive cell fold into the reduced Brillouin zone, increasing the bands' multiplicity. Furthermore, high-energy valleys originally situated at the boundary of the original Brillouin zone are mapped to the center ($\Gamma$ point) of the folded zone.

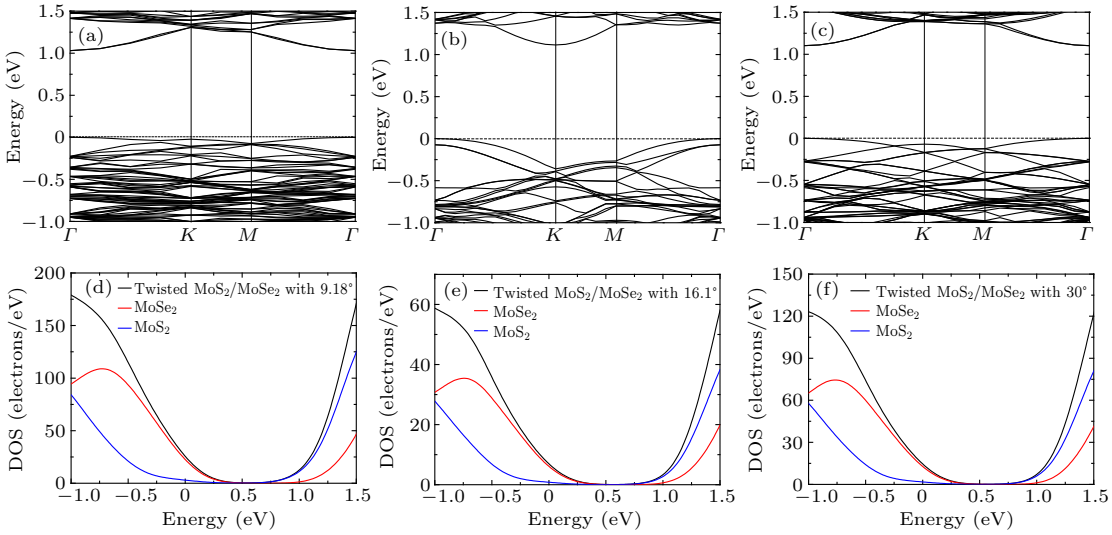


**Fig. 5.** Band structures of twisted $MoS_2/MoSe_2$ heterobilayers at twist angles of (a) 9.18°, (b) 16.1° and (c) 30°, where the valence band maximum is set to 0 eV. Total density of states (DOS) for twist angles of (d) 9.18°, (e) 16.1° and (f) 30°. The black curves denote the total DOS of the heterobilayer; red and blue curves denote the local DOS projected onto the $MoSe_2$ and $MoS_2$ layers, respectively.

The DOS of twisted $MoS_2/MoSe_2$ heterobilayers, as well as the layer-projected local DOS (LDOS) for the $MoSe_2$ and $MoS_2$ layers at twist angles of 9.18°, 16.1°, and 30°, are presented in Figs. 5(d)–5(f). Our analysis reveals that these heterobilayers exhibit a distinct type-II band alignment. In this configuration, the CBM and VBM are spatially localized in different layers: the VBM is predominantly contributed by the $MoSe_2$ layer, while the CBM is mainly situated within the $MoS_2$ layer. This alignment facilitates the spatial separation of photogenerated electrons and holes, which effectively suppresses carrier recombination and is advantageous for enhancing the performance of optoelectronic devices. The inherent band offset between $MoS_2$ and $MoSe_2$ drives interfacial charge transfer, establishing a built-in electric field that further promotes efficient carrier separation. These findings are consistent with previously reported theoretical and experimental studies.[38,39]

To gain deeper insight into the interfacial charge redistribution, we further calculate the work function $\Phi$. It is important to note that the work function, defined as $\Phi = E_{Vac} - E_F$, is the minimum energy required to extract an electron from the Fermi energy level $E_F$ with reference to the vacuum energy level $E_{Vac}$, and provides critical information about the photoelectric emission efficiency of semiconductors.[40,41] The work functions of isolated $MoS_2$ and $MoSe_2$ monolayers, summarized in Table 3, agree well with values reported in previous studies.[42–44] The lower work function of $MoSe_2$ compared with $MoS_2$ is primarily due to the reduced electronegativity of Se relative to S. This difference in electronegativity facilitates electron transfer from the $MoSe_2$ layer to the $MoS_2$ layer upon formation of heterobilayers. The computed work functions of the twisted $MoS_2/MoSe_2$ heterobilayers at angles

of 9.18°, 16.1°, 30°, 43.9° and 50.82° are also presented in Table 3. The results indicate that the twist angle has a minimal influence on the work function of $MoS_2$/$MoSe_2$ heterobilayers. This behavior can be attributed to the small lattice mismatch between $MoS_2$ and $MoSe_2$, which results in a long-period moiré potential with low amplitude. Such weak potential modulations are insufficient to alter the large-scale interlayer charge transfer dominated by the intrinsic band offset. As a consequence, the macroscopic work function remains largely invariant. The introduction of a twist angle introduces only minor perturbations to the system without inducing substantial changes in its electronic environment.

**Table 3.** Calculated work functions (in eV) of isolated monolayers and $MoS_2$/$MoSe_2$ heterobilayers at various twist angles.

| | $\theta$ (°) | | | | |
|---|---|---|---|---|---|
| | 9.18 | 16.1 | 30 | 43.9 | 50.82 |
| $MoS_2$ | 5.757 | 5.787 | 5.763 | 5.750 | 5.785 |
| $MoSe_2$ | 5.272 | 5.303 | 5.280 | 5.304 | 5.302 |
| $MoS_2$/$MoSe_2$ | 5.348 | 5.352 | 5.332 | 5.309 | 5.345 |

### 3.3. Elastic properties

In practical applications, the mechanical properties of 2D materials are of crucial importance and they often exhibit exceptional behavior. The evaluation of these properties is fundamentally based on the determination of elastic constants, which can be derived from the constitutive stress–strain relationship, yielding the in-plane elastic constants $C_{ij}$ (where $i$, $j = 1, 2, 6$).[45] For materials with hexagonal or triangular lattice symmetry, there are four nonzero elastic constants in the 2D regime: $C_{11}$, $C_{22}$, $C_{12}$, and $C_{66}$. However, due to the structural isotropy of twisted $MoS_2$/$MoSe_2$ heterobilayers, $C_{22}$ is equivalent to $C_{11}$, and $C_{66}$ is equal to $(C_{11}-C_{12})/2$. Thus, only two independent elastic constants, $C_{11}$ and $C_{12}$, are sufficient to characterize their linear elastic response. The in-plane stiffness $B_{2D}$ and shear modulus $G_{2D}$ are defined as follows:[46]

$$B_{2D} = \frac{C_{11}+C_{12}}{2}, \tag{10}$$

$$G_{2D} = C_{66} = \frac{C_{11}-C_{12}}{2}. \tag{11}$$

Additionally, the elastic behavior can be described by the 2D Young's modulus $Y_{2D}$ and Poisson's ratio $\nu_{2D}$, expressed in terms of the elastic constants as

$$Y_{2D} = \frac{C_{11}^2 - C_{12}^2}{C_{11}}, \tag{12}$$

$$\nu_{2D} = \frac{C_{12}}{C_{11}}. \tag{13}$$

To investigate the influence of twist angle on elastic properties, we summarize the independent elastic constants $C_{11}$ and $C_{12}$, plane moduli $B_{2D}$, shear moduli $G_{2D}$, Young's moduli $Y_{2D}$ and Poisson's ratio $\nu_{2D}$ for twisted $MoS_2$/$MoSe_2$ heterobilayers in Table 4. According to the Born–Huang criteria,[47] a mechanically stable 2D structure must satisfy $C_{11} > |C_{12}|$ and $C_{66} > 0$. Our results confirm that all twisted configurations satisfy these conditions and are therefore mechanically stable.

The elastic parameters of $MoS_2$/$MoSe_2$ heterobilayers are modulated by the twist angle, although the overall variation amplitude is limited. As summarized in Table 4, the elastic constants, plane moduli, shear moduli, Young's modulus and Poisson's ratio all display minor fluctuations across different angles, with most changes confined to within ±3%. The estimated Young's modulus values (231.76–240.42 N/m) are close to the experimentally measured value for bilayer $MoS_2$ ($260 \pm 70$ N/m)[48] and the theoretical value for twisted bilayer $MoS_2$.[27] Notably, these values surpass those reported for other 2D materials such as silicene (60 N/m) and phosphorene (23–92 N/m),[8] indicating the superior rigidity of twisted $MoS_2$/$MoSe_2$ heterobilayers.

A notable exception occurs at $\theta = 30°$, where $C_{11}$, $C_{66}$, $B_{2D}$, $G_{2D}$, and $Y_{2D}$ reach their maximum values, while $C_{12}$ and $\nu_{2D}$ decrease to minimum values. This anomalous behavior is primarily ascribed to the distinctively flat interfacial geometry realized at this angle, characterized by minimal layer spacing variation ($\Delta d$, Fig. 3), which promotes uniform interlayer stress distribution and thereby enhances in-plane bond stiffness and interlayer shear resistance. Consequently, the relaxed interfacial configuration is a critical factor governing the angular dependence of elastic properties in twisted $MoS_2$/$MoSe_2$ heterobilayers.

**Table 4.** Twist angle $\theta$, elastic constants $C_{11}$ and $C_{12}$, plane moduli $B_{2D}$, shear moduli $G_{2D}$, Young's modulus $Y_{2D}$ and Poisson's ratio $\nu_{2D}$ of $MoS_2$/$MoSe_2$ heterobilayers at various twist angles.

| | $\theta$ (°) | | | | |
|---|---|---|---|---|---|
| | 9.18 | 16.1 | 30 | 43.9 | 50.82 |
| $C_{11}$ (N/m) | 251.79 | 250.37 | 256.15 | 248.69 | 251.62 |
| $C_{12}$ (N/m) | 66.99 | 67.16 | 63.47 | 64.89 | 66.34 |
| $C_{66}$ (N/m) | 92.40 | 91.61 | 96.34 | 91.90 | 92.64 |
| $B_{2D}$ (N/m) | 159.39 | 158.77 | 159.81 | 156.79 | 158.97 |
| $G_{2D}$ (N/m) | 92.40 | 91.61 | 96.34 | 91.90 | 92.64 |
| $Y_{2D}$ (N/m) | 233.96 | 232.35 | 240.42 | 231.76 | 234.11 |
| $\nu_{2D}$ | 0.266 | 0.268 | 0.248 | 0.261 | 0.264 |

**Table 5.** Calculated elastic properties of $MoS_2$ and $MoSe_2$ monolayers and homobilayers (AA stacking). The elastic constants $C_{11}$ and $C_{12}$ are in units of N/m. The 2D Young's modulus is calculated as $(C_{11}^2 - C_{12}^2)/C_{11}$.

| System | $C_{11}$ (N/m) | $C_{12}$ (N/m) | $Y_{2D}$ (N/m) | Reference |
|---|---|---|---|---|
| $MoS_2$ monolayer | 132.7 | 28.6 | 126.5 | [46] (our work) |
| | 134.89 | 32.03 | 127.3 | [45] |
| | 132.7 | 33 | 124.5 | [49] |
| $MoSe_2$ monolayer | 117.5 | 24.9 | 112.2 | This work |
| | 110.7 | 25.66 | 104.8 | [45] |
| | 106.9 | 25.6 | 103.9 | [49] |
| $MoS_2$ bilayer | 266.3 | 75.8 | 244.7 | This work |
| | | | 249.9 | [19] |
| $MoSe_2$ bilayer | 245.5 | 67.2 | 227.1 | This work |
| | | | 213.4 | [49] |

For reference, the calculated elastic constants and 2D Young's modulus of the pristine $MoS_2$ and $MoSe_2$ monolayers and bilayers are provided in Table 5. Our results are consistent with previous reports,[45,49] validating our computational approach. As expected, the in-plane stiffness of $MoSe_2$ is lower than that of $MoS_2$ due to its longer bond lengths and weaker ionic interactions, and the elastic properties of the twisted $MoS_2$/$MoSe_2$ heterobilayers lie between those of the two parent materials and are effectively tuned by the twist angle.

## 4. Conclusions

In this work we have constructed five commensurate twisted $MoS_2$/$MoSe_2$ heterobilayers with distinct twist angles of 9.18°, 16.1°, 30°, 43.9° and 50.82° using the coincidence lattice method and systematically investigated their structural, electronic and elastic properties through first-principles calculations. Full structural relaxations have been performed to optimize both the in-plane and out-of-plane atomic configurations. Our results reveal a remarkable twist-angle-dependent interfacial morphology: while most angles exhibit significant corrugation with the largest interlayer spacing fluctuation occurring at 9.18° and 50.82°, the 30° heterobilayer demonstrates exceptional interfacial flatness, approaching an ideal planar geometry. A more pronounced corrugation is reflected by a larger variation between $d_{\min}$ and $d_{\max}$, which can enable the system to maximize the fractional area of strongly coupled regions with low-energy stacking domains (e.g., AB-1) while minimizing that of weakly coupled regions with high-energy stacking domains (e.g., AA). The structural behavior governs the binding energy variation. Electronic structure analyses, including DOS and layer projected LDOS, reveal that the band structure can be tuned between direct and indirect band gap behaviors by varying the twist angle. The VBM and CBM are spatially localized in the $MoSe_2$ and $MoS_2$ layers, respectively, confirming a type-II band alignment conducive to efficient charge separation. The elastic properties, characterized via the constitutive stress–strain relationship, show that the elastic constants, plane moduli, shear moduli, Young's modulus and Poisson's ratio exhibit only minor variations (±3%) across different twist angles, indicating robust mechanical stability. Remarkably, the Young's moduli of these heterobilayers exceed those reported for other 2D materials such as silicene and phosphorene. These findings not only establish the structure–property relationships in twisted $MoS_2$/$MoSe_2$ heterobilayers but also highlight their potential as a tunable platform for advanced optoelectronic applications.

## Acknowledgements

L. Xue was supported by the Hubei Provincial Natural Science Foundation and Xianning of China (Grant No. 2025AFD397) and the National Natural Science Foundation of China (Grant No. 11747044). C. B. Hua was supported by the National Natural Science Foundation of China (Grant No. 12304539) and the Doctoral Research Start-Up Fund of Hubei University of Science and Technology (Grant No. BK202316). We sincerely thank Professor Lin Yi of Huazhong University of Science and Technology for Providing the Computing Platform.

## References

[1] Castellanos-Gomez A, Duan X, Fei Z, Gutierrez H R, Huang Y, Huang X, Quereda J, Qian Q, Sutter E and Sutter P 2022 *Nat. Rev. Method. Prime.* **2** 58
[2] Wang P, Jia C, Huang Y and Duan X 2021 *Matter* **4** 552
[3] Novoselov K, Mishchenko A, Carvalho A and Castro Neto A H 2016 *Science* **353** aac9439
[4] Rong Z Y and Kuiper P 1993 *Phys. Rev. B* **48** 17427
[5] Wu F, Lovorn T and MacDonald A H 2016 *Phys. Rev. Lett.* **118** 147401
[6] Li T, Jiang S, Shen B, Zhang Y, Li L, Tao Z, Devakul T, Watanabe K, Taniguchi T, Fu L, Shan J and Mak K F 2021 *Nature* **600** 641
[7] Cao Y, Valla F, Fang S, Watanabe K, Taniguchi T, Kaxiras E and Jarillo-Herrero P 2018 *Nature* **556** 43
[8] Gupta N, Rani S, Kumari P, Ahuja R and Ray S J 2023 *Carbon* **215** 118437
[9] Chen S and Pan Y 2022 *Appl. Surf. Sci.* **599** 154041
[10] Wang Y, Sarkar S, Yan H and Chhowalla M 2024 *Nat. Electron.* **7** 638
[11] Zhao B, Shen D, Zhang Z, Lu P, Hossain M, Li J, Li B and Duan X 2021 *Adv. Funct. Mater.* **31** 2105132
[12] Roy S, Joseph A, Zhang X, Bhattacharyya S, Puthirath A B, Biswas A, Tiwary C S, Vajtai R and Ajayan P M 2024 *Chem. Rev.* **124** 9376
[13] Götting N, Lohof F and Gies C 2022 *Phys. Rev. B* **105** 165419
[14] Zhu J, Chou Y Z, Xie M and Das Sarma S 2025 *Phys. Rev. B* **111** L060501
[15] Regan E C, Wang D, Paik E Y, Zeng Y, Zhang L, Zhu J, MacDonald A H, Deng H and Wang F 2022 *Nat. Rev. Mater.* **7** 778
[16] Angeli M and MacDonald A H 2021 *Proc. Natl. Acad. Sci. USA* **118** e2021826118
[17] Vitale V, Atalar K, Mostofi A A and Lischner J 2021 *2D Mater.* **8** 045010
[18] Li S Y, Xu Z, Wang Y, Han Y, Watanabe K, Taniguchi T, Song A, Ma T B, Gao H J, Jiang Y and Mao J 2024 *Phys. Rev. Lett.***133** 196401
[19] Arnold F M, Ghasemifard A, Kuc A, Kunstmann J and Heine T 2023 *2D Mater.* **10** 045010
[20] Li W, Brumme T and Heine T 2024 *NPJ 2D Mater. Appl.* **8** 43
[21] Zhao S, Li Z, Huang X, Rupp A, Göser J, Vovk I A, Kruchinin S Y, Watanabe K, Taniguchi T, Bilgin I and Baimuratov A S 2023 *Nat. nanotechnol.* **8** 572
[22] Lu N, Guo H, Zhuo Z, Wang L, Wu X and Zeng X C 2017 *Nanoscale* **9** 19131
[23] Naik S, Naik M H, Maity I and Jain M 2022 *Comput. Phys. Commun.* **271** 108184
[24] Uchida K, Furuya S, Iwata J I and Oshiyama A 2014 *Phys. Rev. B* **90** 155451
[25] Koda D S, Bechstedt F, Marques M and Teles L K 2016 *J. Phys. Chem. C* **120** 10895
[26] Lopes dos Santos J M B, Peres N M R and Castro Neto A H 2007 *Phys. Rev. Lett.* **99** 256802
[27] Ren Y M, He J R, Hu Z L, Hu Y H, Hua C B and Xue L 2025 *Vacuum* **235** 114146
[28] Li P, Lu J, Wang W Y, Sui X, Zou C, Zhang Y and Liu W 2021 *Nanoscale* **13** 16234
[29] Sachin S, Rani S, Kumari P, Kar S and Ray S J 2023 *Appl. Phys. A* **129** 46
[30] Segall M D, Lindan P J, Probert M A, Pickard C J, Hasnip P J, Clark S J and Payne M C 2002 *J. Phys. Condens. Mat.* **14** 2717
[31] Pfrommer B G, Côté M, Louie S G and Cohen M L 1997 *J. Comput. Phys.* **131** 233
[32] Perdew J P, Burke K and Ernzerhof M 1997 *Phys. Rev. Lett.* **77** 3865
[33] Vanderbilt D 1990 *Phys. Rev. B* **41** 7892
[34] Grimme S 2006 *J. Comput. Chem.* **27** 1787
[35] Monkhorst H J and Pack J D 1976 *Phys. Rev. B* **13** 5188

[36] Van Der Zande A M, Kunstmann J, Chernikov A, Chenet D A, You Y, Zhang X, Huang P Y, Berkelbach T C, Wang L, Zhang F, Hybertsen M S, muller D A, Reichman D R, Heinz T F and Hone J C 2014 *Nano Lett.* **14** 3869
[37] Gupta N, Sachin S, Kumari P, Rani S and Ray S J 2024 *RSC Adv.* **14** 2878
[38] Constantinescu G C and Hine N D 2015 *Phys. Rev. B* **91** 195416
[39] Ceballos F, Bellus M Z, Chiu H Y and Zhao H 2014 *ACS Nano* **8** 12717
[40] Tsoeu S E, Opoku F and Govender P P 2020 *SN Appl. Sci.* **2** 341
[41] Nguyen C Q, Ang Y S, Nguyen S T, Hoang N V, Hung N M and Nguyen C V 2022 *Phys. Rev. B* **105** 045303
[42] Liu J, Jin Y, Lei B, Zhao X, Huang Y, Zhang L and Zhu Y 2024 *Catalysts* **14** 678
[43] Wang Y, Liu T, Tian W, Zhang Y, Shan P Y, Chen Y J, Wei W H, Yuan H K and Cui H 2020 *RSC Adv.* **10** 41127
[44] Li S, Zang W, Liu X, Pennycook S J, Kou Z K, Yang C H, Guan G and Wang J 2019 *Chem. Eng. J.* **359** 1419
[45] Zeng F, Zhang W B and Tang B Y 2015 *Chin Phys B* **24** 097103
[46] Xue L, Ren Y M, He J R, Zhao Y, Xu S L, Hu Y H and Hua C B 2024 *Results Phys.* **57** 107418
[47] Born M and Huang K 1996 *Dynamical Theory of Crystal Lattices* (Oxford: Oxford University Press)
[48] Bertolazzi S, Brivio J and Kis A 2011 *ACS Nano* **5** 9703
[49] Çakır D, Peeters F M and Sevik C 2014 *Appl. Phys. Lett.* **104** 203110